PCCP

ROYAL SOCIETY OF CHEMISTRY

PAPER

View Article Online
View Journal | View Issue

Check for updates

Cite this: *Phys. Chem. Chem. Phys.*, 2023, **25**, 6288

Effects of high pressure on the lattice structure and electrical transport properties of BiOI

Xiaotong Zhang,[a] Dawei Jiang,[a] Yonghao Han*[a] and Yang Gao*[bc]

HPSTAR
1642-2023

Received 8th November 2022,
Accepted 14th January 2023

DOI: 10.1039/d2cp05231h

rsc.li/pccp

To reveal the pressure effects on BiOX semiconductors, we performed in-situ Raman spectroscopy and electrical transport measurements on BiOI up to 26.1 GPa and 19.2 GPa. BiOI showed good structural stability, while the electron conduction characteristics maintained dominance throughout the pressure range. The influence of grain boundary conduction disappeared at pressures above 9.2 GPa. With pressure elevation, the pressure-induced lattice fragmentation and grain refinement introduced a large number of relevant levels in the energy gap and resulted in a significant increase in the conductivity of BiOI under compression. The conductivity increased by 10^6 at 19.2 GPa from the initial value and maintained an increase of 10^2 after depressurization until ambient conditions were attained. At the same time, the space charge polarization of the crystal interface layer became weaker with pressure elevation resulting in a decrease in the relative permittivity of BiOI. The calculation results of the complex permittivity showed that the frequency of orientation polarization response decreases with pressure elevation, and the complex permittivity becomes constant in the high-frequency region. Our work proves that pressure could significantly increase the carrier concentration and mobility, thus effectively improving the conductivity of BiOX semiconductors.

1 Introduction

In recent years, the demand for solar energy to alleviate energy and environmental stress has led to extensive research on new BiOX (X = F, Cl, Br, and I) semiconductor materials.[1–3] BiOX semiconductors are V-VI-VII semiconductor materials with a PbFCl-type layered tetragonal structure. BiOI, as a representative, has good optical, electrical, and magnetic properties and is mainly used as an ionic conductor and ferroelectric material and has applications in photocatalysis and other fields.[4–8]

The pressure effects on BiOX materials have attracted much interest due to their robust layered structure at lower pressures. In the typical layered crystal structure of BiOX, $[Bi_2O_2]^{2+}$ and X^{n-} along the [001] direction, weak van der Waals forces connect two adjacent X^{n-} layers indicating that the ionic radius and electronegativity of X^{n-} significantly affect the phase transition behavior of BiOX materials under higher pressures. Xu *et al.* predicted that BiOI has no phase transition at pressures below 60 GPa.[9] Zhao *et al.* found an isomorphic phase transition of the $P4/nmm$ phase of BiOCl up to 40 GPa using *in situ* high-pressure angle-dispersive X-ray diffraction techniques and the first-principle calculations.[10] Zhou *et al.* predicted that BiOF shows transitions from the initial PbFCl phase to the $Pnma$, $P\bar{3}m1$, and $Cmcm$ phases up to 300 GPa.[11] However, systematic experimental studies of the effects of pressure on its electrical transport properties are still lacking.

Currently, BiOI has become a hotspot due to its easy stripping layer structure, relatively narrow band gap (2.2eV), small effective electron mass, low synthesis temperature, good absorption characteristics in the visible light range and the best photocatalytic activity for the degradation of organic pollutants.[12,13] However, most of the research on BiOI is mainly focused on doping modification, emphasizing the improvement of its carrier mobility efficiency.[14–16] These studies undoubtedly offer advantages for different optical applications of BiOI. However, as an effective means to regulate the structure and properties of materials, pressure can better display the relationship between the structure and the properties.[17–20] For example, by compressing multiple layers of ReS_2, Yan *et al.* found that pressure can be used to effectively modulate the photoelectric properties of transition metal disulphide (TMDS) by controlling the atomic displacement, which has potential applications in the design and manufacture of various stacked nanoscale devices.[21] Tong *et al.* showed that the frequency of the input signal could regulate the electric transmission operation of Bi_2O_3 under high pressure. Bi_2O_3 behaves like an ionic solid electrolyte at high frequencies but as an electronic resistor at low frequencies.[22] These studies prove that research using

---

[a] *State Key Laboratory of Superhard Materials, Jilin University, Changchun 130012, China. E-mail: hanyh@jlu.edu.cn*

[b] *Center for High Pressure Science and Technology Advanced Research, Beijing 10094, China. E-mail: yang.gao@hpstar.ac.cn*

[c] *Shanghai Institute of Laser Plasma, Shanghai 200000, China*

high pressure can reveal more novel properties of materials and provide new possibilities for expanding and improving the application of materials. A systematic study of the pressure effects on BiOI's electrical transport properties would better reveal the potential and correlate pressure with the further exploration of BiOX semiconductors.

Herein, we prepared a BiOI sample with a layered structure by hydrothermal synthesis, examined its behaviour under compression by recording its Raman spectra, and monitored its electrical performance at different pressures through impedance measurements in a diamond anvil cell. The result proved that pressure could effectively regulate the conductivity and permittivity of BiOI, which is one step further into understanding the properties of BiOX materials under compression.

2 Experimental details

2.1 Sample preparation and characterization

The experimental samples used in this paper are BiOI powder prepared by hydrothermal synthesis. All reagents used in the synthesis are from Aladdin Reagent Co. Ltd. In practice, we slowly added $Bi(NO_3)_3 \cdot 5(H_2O)$ (AR, 99.0%) to a glycol solution of KI (AR, 99.0%) until the molar ratio between Bi and I reached 1. The mixture was stirred for half an hour at room temperature and then poured into a 25 ml Teflon-lined high-pressure reactor. The reactor was kept in a muffle furnace at 160 °C for 7 hours and cooled to room temperature before the obtained pellet was collected, washed with ethanol and distilled water, dried, and then ground for use.

We used X-ray diffraction (XRD) and scanning electron Microscopy (SEM) measurements to characterize the initial sample. Specifically, for XRD and the SEM measurements a Shimadzu XRD-6000 diffractometer and a MIRA3LMH scanning electron microscope were used, respectively. The X-ray source was a Ni-filtered Cu target with a wavelength of 1.5405 Å.

2.2 Raman spectroscopy and impedance spectroscopic measurements

The pressure generating apparatus in this work was a diamond anvil cell (DAC) equipped with 300 μm diameter anvils, a 130 μm diameter sample chamber and a T-301 stainless steel gasket (200 μm initial thickness and 22.1 μm final thickness). The sample thickness under pressure was determined using a micrometer. Ruby fluorescence techniques were used to calibrate the pressure in this work.[23] Parallel plate electrodes were fabricated on the DAC to measure the impedance spectrum.[18] We used two thin platinum foils as the electrodes and attached them to the top and bottom of the sample. And a layer of a mixture of Al_2O_3 and epoxy was applied to insulate the electrode from the gasket (as shown in Fig. 1). We used a no pressure-transmitting medium throughout the experiment.

The Raman spectroscopic measurements were conducted using a homemade Raman system equipped with a LabRAM HR Evolution Raman spectrometer from the HORIBA company and a tunable solid-state laser with a wavelength of 532 nm. The Raman spectroscopy measurement range extends from ambient pressure to 26.1 GPa with approximate intervals of 1 GPa. The impedance spectroscopic measurements were performed using a Solartron 1260 impedance analyzer and a Solartron 1296 dielectric interface meter. The sinusoidal AC voltage was 1V, and the frequency was from 10^{-1} Hz to 10^{-6} Hz. The pressure range for impedance measurements was from ambient pressure to 19.2 GPa with approximate intervals of 1 GPa.

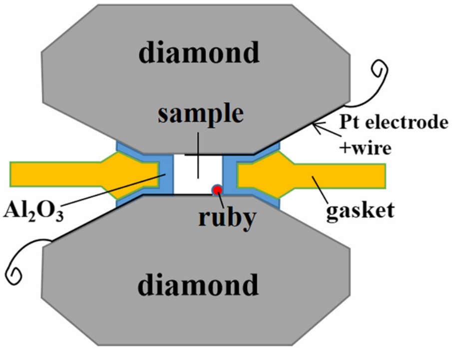

Fig. 1 Schematic diagram of the DAC setup.

It is worth noting that the Raman spectroscopic measurements and impedance spectroscopic measurements were performed in two separate runs but using the same DAC. The insulation layer and electrodes were not inserted in the DAC for Raman spectroscopic measurements.

3 Results and discussion

3.1 Characterization of the initial sample

The XRD pattern of the initial sample shows that the powder had a tetragonal structure with the space group *P*4/*nmm*. The position of the diffraction peaks corresponds to the standard PDF of BiOI (PDF#00-010-0445), whose lattice parameters are a = 3.994 (Å), b = 3.994 (Å), and c = 9.149 (Å) under ambient conditions (Fig. 2(a)). Therefore, we determined that the initial sample was pure BiOI. Fig. 2(b) shows an SEM image of the prepared BiOI powder. The image shows that the powder consisted of rose-like microspheres with a 2–3 μm diameter. These characteristic microspheres are self-assembled from layered microsheets and essential for the light absorption,

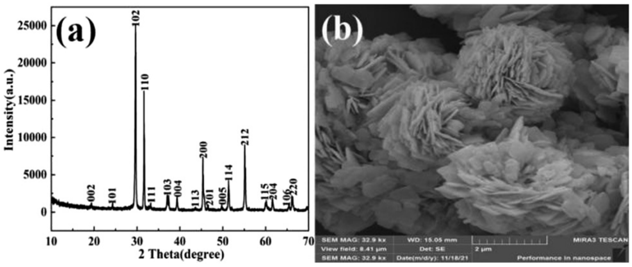

Fig. 2 Characterization of the initial sample: (a) an XRD pattern and (b) an SEM image of the prepared sample under ambient conditions.

carrier separation, transport efficiency, and redox properties of BiOX materials.[24]

3.2 High-pressure lattice structure analysis

Under ambient conditions, the two characteristic Raman peaks at 101.9 cm^{-1} and 149.0 cm^{-1} respectively correspond to the Bi–I bond's internal stretching modes, A_{1g} and E_g. The peaks at 65.8 cm^{-1} and 85.2 cm^{-1} respectively originate from the Bi–I bond's external stretching modes, A_{1g} and B_{1g}.[25] With increasing pressure, the Raman peaks blueshift while their intensity gradually decreases. The blue shift originates from the enhanced intermolecular force due to the reduced intermolecular distance under compression (Fig. 3(a)).[26]

The B_{1g}(ex.) and E_g(in.) tended to merge at 26.1 GPa (at the red double arrow), indicating that the two modes shifted at different speeds with pressure. Raman displacements are linearly fitted by the Gaussian fitting method. As shown in Fig. 3(b), no abnormal behavior emerged at the given pressure point, indicating that no structural phase transition occurred throughout the experiment. The increase in the shift (Fig. 3(b)) and the FWHM (Fig. 3(c)) of the Raman modes with pressure is due to the possible lattice breaking and grain refinement caused by pressure elevation.[27,28]

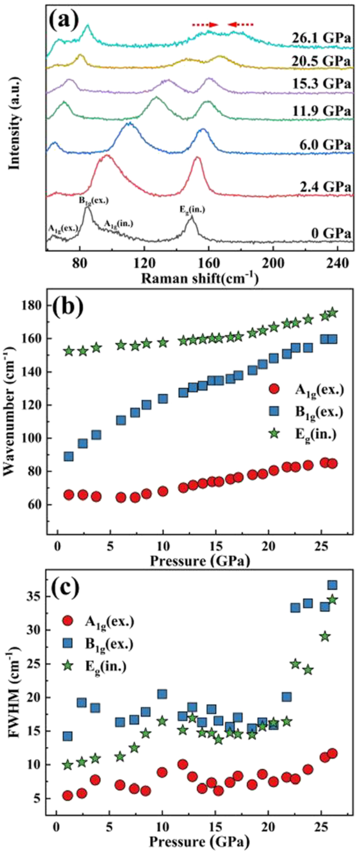

Fig. 3 Raman spectroscopic results of BiOI, (a) selected Raman spectra of BiOI at pressures, (b) evolution of Raman shifts of BiOI with pressure, and (c) evolution of the FWHM of Raman peaks of BiOI with pressure.

In conclusion, no apparent anomaly has emerged in the Raman spectroscopic measurements of BiOI at high pressure, which further supports that the prepared sample is pure BiOI.

3.3 High-pressure AC impedance spectrum analysis

To determine the conduction type of BiOI and understand the mechanism behind it, we plotted the Nyquist plot of BiOI in $Z' \sim \omega^{-1/2}$ at 0.9 GPa (Fig. 4(a)). The low-frequency region Z' and $\omega^{-1/2}$ are in a nonlinear relationship, indicating no ionic conductivity in BiOI. Considering the large gap between the grain and grain boundary conduction, we used the Z'–Z''/f representation to process the impedance data of BiOI at 0.9 GPa (Fig. 4(b)).[29] According to the analysis, three straight segments with different slopes correspond to the contribution of the grain, grain boundary, and electrode part from left to right. The linear gradient of the corresponding electrode part is always 0, indicating that the relaxation frequency of the electrode part remains 0. Therefore, we did not observe the semicircle of the electrode in the impedance spectrum.

Fig. 5(a)–(c) shows the Nyquist plot of BiOI at different pressures. BiOI exhibits a pure electron conduction process below 19.2 GPa. At lower pressures (ambient to 8.3 GPa), the Nyquist plot of BiOI consisted of two arcs, indicating that the conduction of BiOI included both the grain's contribution and the grain boundary's contibution. The arc to the left represents the grain contribution in the high-frequency region, and the arc to the right represents the grain boundary contribution in the low-frequency region. As shown in Fig. 5(a), at low pressures (0–3.4 GPa), the hindering effect of the grain boundary on carriers is dominant, that is, the grain boundary resistance is prevalent. In this case, the scattering of the electron is weaker inside the grains than at the grain boundaries. With pressure elevation (5.3–8.3 GPa), both arcs gradually shift to the right, forming a double-arc structure, as shown in Fig. 5(b). The impedance spectrum gradually turns into a single arc with a further increase in pressure, as shown in Fig. 5(c). The transformation indicates that the scattering effect of grains on electrons becomes dominant. In contrast, the scattering effect of carriers at grain boundaries decreases much faster than that of grains until it disappears. At the same time, the intercept between the semi-arc of the grain and the real axis Z' decreases gradually, indicating that the resistance of the grain and the grain boundary decreases with pressure.

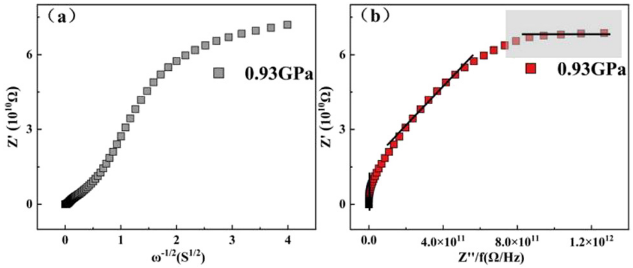

Fig. 4 AC impedance spectrum of BiOI, (a) $Z' \sim \omega^{-1/2}$ plot at 0.9 GPa and (b) Z'–Z''/f plot at 0.9 GPa.

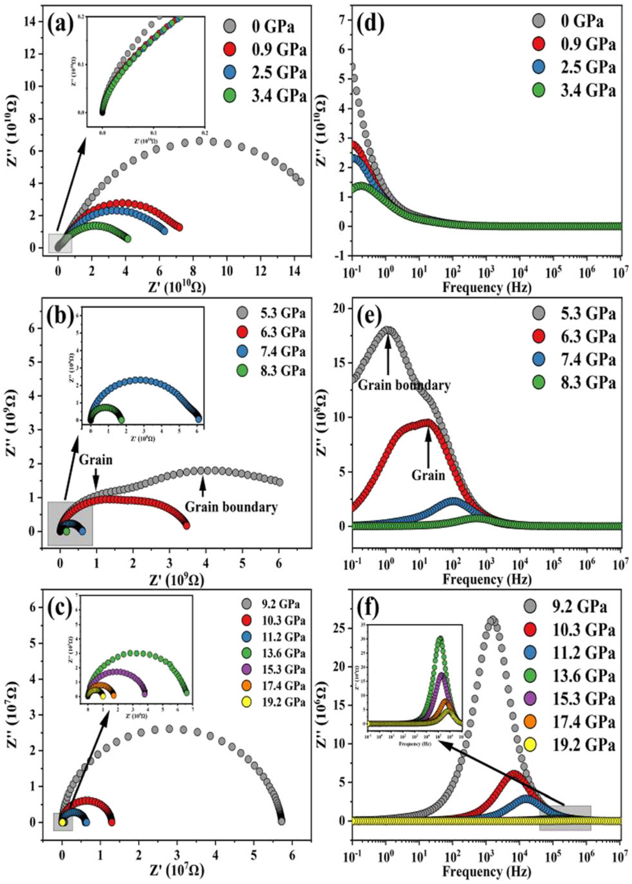

Fig. 5 Nyquist plots of the BiOI impedance spectrum in pressure ranges (a) from ambient to 3.4 GPa, (b) from 5.3 to 8.3 GPa, and (c) from 9.3 to 19.2 GPa. And the Bode plots of the BiOI impedance spectrum in pressure ranges (d) from ambient to 3.4 GPa, (e) from 5.3 to 8.3 GPa, and (f) from 9.2 to 19.2 GPa.

Fig. 5(d)–(f) shows the Bode diagrams of the BiOI that describe the relationship between the imaginary part Z'' and the frequency at different pressures. The evolution of the Bode diagrams with pressure splits into two stages. Two relaxation peaks emerge below 9.2 GPa, corresponding to the grain boundary's low-frequency relaxation peak and the grain's high-frequency relaxation peak (Fig. 5(d) and (e)). At the initial stage of pressure loading (0–3.4 GPa), only one relaxation peak appears in the low-frequency region with a pressure increase, indicating a large number of crystal gaps in the sample. The accumulating number of carriers trapped within the crystal gaps resulted in a relatively high initial resistance detected in the experiment. Upon compression, the crystal gaps gradually evolve into grain boundaries and thus result in a double peak pattern shown in Fig. 5(e). Meanwhile, grain boundaries' resistance decreases rapidly when the scattering effect of grains on carriers gradually becomes dominant with pressure elevation. The relaxation peak representing the grain boundary effect decays rapidly as pressure increases. And the total impedance value decreases with pressure, confirming that the resistance decreases continuously, as revealed in the Nyquist plot. At pressures above 9.2 GPa (Fig. 5(f)), the grain boundary relaxation peak disappears, indicating that the scattering effect of the grains on carriers completely dominates the resistance of BiOI.[30] When the pressure reaches 19.2GPa, the resistance of the sample has decreased by 10^6 times compared to the initial resistance.

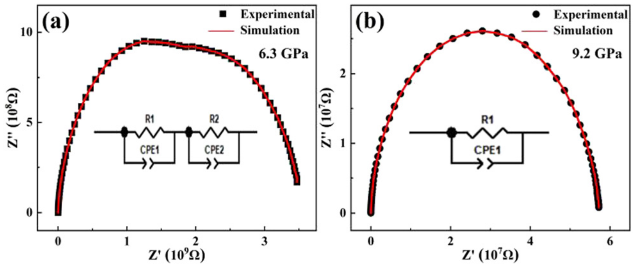

Fig. 6 Nyquist plots and equivalent circuits of BiOI at (a) 6.3 GPa and (b) 9.2 GPa.

To further analyze the effect of pressure on the electrical transport properties of BiOI, we fitted the impedance spectra at 6.3 and 9.2 GPa using ZView2 impedance analysis software. Fig. 6 shows the Nyquist diagrams with fitting results and the equivalent circuits at different pressures. At 6.3 GPa, the impedance spectrum showed a double-arc structure with different radii indicating a combined grain and grain boundary conductivity (Fig. 6(a)). Thus, the equivalent circuit follows a serial connection of two R and CPE parallel circuits, representing the grain and grain boundary's electron conduction process, where $R1$, $R2$, CPE1, and CPE2 correspond to the resistance and the charge/discharge process between electrodes of the grain and grain boundary, respectively. At 9.2 GPa, the equivalent circuit of BiOI follows a parallel connection of resistance (R) and constant phase angle element (CPE) pattern (Fig. 6(b)). The impedance spectrum shows a single-arc structure whose corresponding impedance spectrum expression is:[31]

$$Z = 1/(1/R + 1/Z_Q) \tag{1}$$

where R and Z_Q represent the transferred electron and the constant phase angle element (CPE), respectively. And Z_Q is given using the following expression:

$$Z_Q = \sigma_Q(j\omega)^{-n} \tag{2}$$

where σ_Q is the coefficient of CPE, ω ($\omega = 2\pi f$) is the angular frequency, and n is the impedance factor, $0 < n < 1$. The conformance of simulated impedance spectra and the experimental data suggest that the equivalent circuit describes the carrier scattering and transport behavior of BiOI well.

Fig. 7(a) shows the contribution of grains and grain boundaries to the total resistance. The total resistance (Fig. 7(b)) decreases with no abrupt change as pressure increases throughout the experiment, which is consistent with the previous results of Raman spectroscopy and the previous calculation results that no pressure-induced phase transition occurred in BiOI.[9] During decompression, the resistance of BiOI gradually recovered but remained two orders of magnitude lower than the initial value after complete depressurization. Besides, the

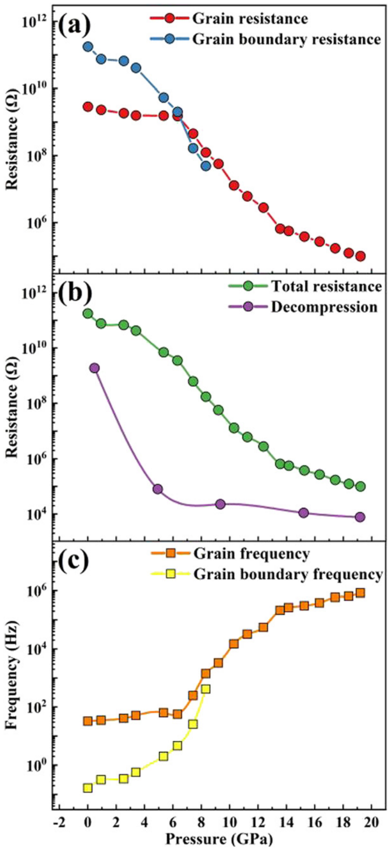

Fig. 7 Evolution of (a) grain resistance and grain boundary resistance with pressure, (b) total resistance with pressure during the pressurization and depressurization processes, and (c) grain frequency and the grain boundary frequency with pressure.

grain boundary resistance didn not show up throughout the decompression process (as shown in Fig. 8). The difference in resistance during the compression and decompression processes is attributed to cube fragmentation and grain refinement under compression. It is well-known that the pressure-induced disruption of cubes can produce abundant boundaries and microstrains in the sample, adding additional energy levels into the band gap and increasing the concentration of free charge carriers.[27,32] The inverse trend of the relaxation frequency of the grain and grain boundaries with pressure indicates a negative correlation between the relaxation time and pressure.

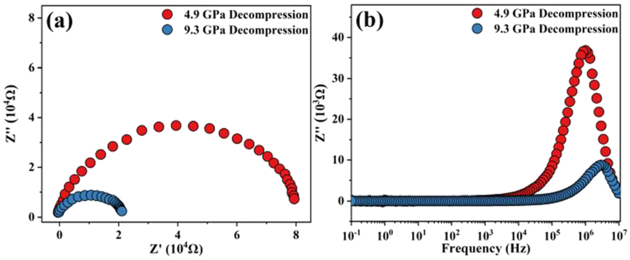

Fig. 8 Comparison of the (a) Nyquist plots and (b) Bode plots at 4.9 and 9.3 GPa during the decompression process.

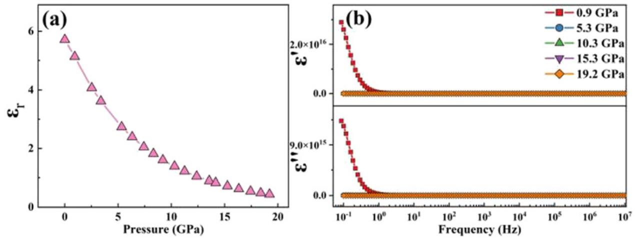

Fig. 9 Evolution of relative permittivity of BiOI with (a) pressure and (b) frequency at selected pressures.

Fig. 9(a) shows the relative permittivity of BiOI (ε_r) as a function of pressure. The following formula is the typical expression of ε_r:

$$\varepsilon_r = d/(2\pi R b \varepsilon_0 f_b S) \tag{3}$$

where d is the sample thickness, ε_0 is the vacuum dielectric constant, and S is the effective electrode area in the experiment. With pressure elevation, ε_r decreases and shows no discontinuity in the entire pressure range. An apparent rate reduction in the pressure-induced variation of ε_r is observed in the experiment and related to the weakening of the spatial charge polarization of the crystal interface layer.[33] To better understand the dielectric properties of BiOI under compression, we also plotted the frequency dependence of the real (ε') and imaginary (ε'') permittivity at different pressures. The calculation formula is as follows:

$$\varepsilon(\omega) = \varepsilon'(\omega) - j\varepsilon''(\omega) \tag{4}$$

$$\varepsilon' = lZ''/2\pi\varepsilon_0 S Z^2 \tag{5}$$

$$\varepsilon'' = lZ'/2\pi\varepsilon_0 S Z^2 \tag{6}$$

where l is the thickness of the sample, ε_0 is the vacuum permittivity, and S is the area of the sample. As shown in Fig. 9(b), when the frequency is below 1 Hz, ε' decreases with the frequency increase due to the decreased contribution of dipoles to polarization. When the frequency exceeds 1 Hz, both ε' and ε'' of BiOI become 0 due to the rapid polarization in the external electric field and the ceased steering polarization of the intrinsic electric moment of the molecule.[34] With a further increase in pressure, both ε' and ε'' of BiOI gradually decrease with frequency, indicating that the dielectric loss of this sample originates from the enhanced electron conduction under compression.

4. Conclusions

BiOI behaved as a pure electron conductor in the experimental pressure range, whose resistance followed a combined pattern of grains and grain boundaries below 9.2 GPa, and a grain pattern at pressures above 9.2 GPa. The pressure effect on the electrical transport properties of BiOI is evident and lasting. Compared with the initial value, the conductivity of BiOI became six orders higher at 19.2 GPa and remained two orders higher after complete depressurization. According to the Raman results, these effects could be attributed to the fragmentation of the lattice, reduced grain size, and increased correlated energy levels in the crystalline gap under compression. The weakening of the space charge polarization at the interfacial layer of the crystal led to a decrease in the relative dielectric constant with pressure. The complex permittivity showed that the frequency of orientation polarization response decreases to 0 at 9.2 GPa in the high-frequency region. The findings of this study fully complement the research on BiOI in the field of high pressure, and the significant improvement of BiOI conductivity provides a new method for regulating the electronic properties of BiOX materials. At the same time, it also provides a reference for applying BiOX layered materials in the direction of high-pressure electrical measurements.

Conflicts of interest

There are no conflicts to declare.

Acknowledgements

This work was supported by the National Natural Science Foundation of China (grant no. 12004015 and 11674404).

References

1 M. Arumugam, T. S. Natarajan, T. Saelee, S. Praserthdam, M. Ashokkumar and P. Praserthdam, Recent developments on bismuth oxyhalides (BiOX; X= Cl, Br, I) based ternary nanocomposite photocatalysts for environmental applications, *Chemosphere*, 2021, **282**, 131054.

2 I. Ahmad, S. Shukrullah, M. Y. Naz, S. Ullah and M. A. Assiri, Designing and modification of bismuth oxyhalides BiOX (X= Cl, Br and I) photocatalysts for improved photocatalytic performance, *J. Ind. Eng. Chem.*, 2022, **105**, 1–33.

3 S. Vinoth, W. J. Ong and A. Pandikumar, Defect engineering of BiOX (X= Cl, Br, I) based photocatalysts for energy and environmental applications: Current progress and future perspectives, *Coord. Chem. Rev.*, 2022, **464**, 214541.

4 A. A. Abuelwafa, R. M. Matiur, A. A. Putri and T. Soga, Synthesis, structure, and optical properties of the nanocrystalline bismuth oxyiodide (BiOI) for optoelectronic application, *Opt. Mater.*, 2020, **109**, 110413.

5 S. T. Navale, Q. Huang, P. Cao, V. B. Patil and F. J. Stadler, Room temperature solid-state synthesis of mesoporous BiOI nanoflakes for the application of chemiresistive gas sensors, *Mater. Chem. Phys.*, 2020, **241**, 122293.

6 M. Sakar, R. M. Prakash, C. M. Hussain and M. V. Shankar, Ferroelectric semiconductors for photocatalytic energy and environmental applications, *Handb. Smart Photocatal. Mater.: Environ., Energy, Emerging Appl. Sustainability*, 2020, 3–19, DOI: 10.1016/B978-0-12-819049-4.00002-7.

7 S. Gao, C. Guo, J. Lv, Q. Wang, Y. Zhang, S. Hou, J. Gao and J. Xu, A novel 3D hollow magnetic Fe_3O_4/BiOI heterojunction with enhanced photocatalytic performance for bisphenol A degradation, *Chem. Eng. J.*, 2017, **307**, 1055–1065.

8 A. A. Putri, S. Kato, N. Kishi and T. Soga, Study of annealing temperature effect on the photovoltaic performance of BiOI-based materials, *Appl. Sci.*, 2019, **9**(16), 3342.

9 W. Zeng, J. Li, L. Feng, H. Pan, X. Zhang, H. Sun and Z. Liu, Synthesis of large-area atomically thin BiOI crystals with highly sensitive and controllable photodetection, *Adv. Funct. Mater.*, 2019, **29**(16), 1900129.

10 J. Zhao, L. Xu, Y. Liu, Z. Yu, C. Li, Y. Wang and Z. Liu, Isostructural phase transition in bismuth oxide chloride induced by redistribution of charge under high pressure, *J. Phys. Chem. C*, 2015, **119**(49), 27657–27665.

11 D. Zhou, C. Pu, C. He, F. Zhang, C. Lu and G. Bao, Pressure-induced phase transition of BiOF: novel two-dimensional layered structures, *Phys. Chem. Chem. Phys.*, 2015, **17**(6), 4434–4440.

12 Z. Xu, H. Li, S. Hu, J. Zhuang, Y. Du and W. Hao, High pressure driven isostructural electronic phase separation in 2D BiOI, *Phys. Status Solidi RRL*, 2019, **13**(6), 1800650.

13 Z. Zhao and W. Dai, Electronic structure and optical properties of BiOI ultrathin films for photocatalytic water splitting, *Inorg. Chem.*, 2015, **54**(22), 10732–10737.

14 Y. Xiang, P. Ju, Y. Wang, Y. Sun, D. Zhang and J. Yu, Chemical etching preparation of the Bi_2WO_6/BiOI p^{-n} heterojunction with enhanced photocatalytic antifouling activity under visible light irradiation, *Chem. Eng. J.*, 2016, **288**, 264–275.

15 J. Zhang, Y. Zheng and H. Zheng, A 2D/3D g-C_3N_4/BiOI heterostructure nano-sphere with oxygen-doped for enhanced visible light−driven photocatalytic activity in environmental remediation, *J. Alloys Compd.*, 2022, **897**, 163044.

16 Y. Xiao, Y. Zhang, L. Ji, J. Yang, J. Wu, T. Jia, Z. Liu, Q. Liu and J. Han, Effect of (La, Ce, Eu) doping on structural, and optical properties of BiOI nanosheets: As a model of photocatalytic activity in heavy metal removal under visible light, *Mater. Chem. Phys.*, 2021, **267**, 124691.

17 Y. Zhao, H. Cui, J. Zhang, Y. Ma, H. Tian, L. Wu, Q. Cui and Y. Ma, Pressure-induced phase transformation of botallackite α-$Cu_2(OH)_3Cl$ with a two-dimensional layered structure synthesized via a hydrothermal strategy, *J. Phys. Chem. C*, 2020, **124**(17), 9581–9590.

18 J. Wang, Y. Yan, H. Liu, G. Zhang, D. Yue, S. Tong, C. Gao and Y. Han, Pressure-induced ionic to mixed ionic and electronic conduction transition in solid electrolyte LaF_3, *Phys. Chem. Chem. Phys.*, 2020, **22**(45), 26306–26311.

19 I. Efthimiopoulos, C. Buchan and Y. Wang, Structural properties of Sb_2S_3 under pressure: evidence of an electronic topological transition, *Sci. Rep.*, 2016, **6**(1), 1–9.

20 L. Zhao, C. Yi, C. Wang, Z. Chi, Y. Yin, X. Ma, J. Dai, P. Yang, B. Yue, J. Cheng, F. Hong, J. Wang, Y. Han, Y. Shi and X. Yu, Monoclinic $EuSn_2$ As_2: A Novel High-Pressure Network Structure, *Phys. Rev. Lett.*, 2021, **126**(15), 155701.

21 Y. Yan, C. Jin, J. Wang, T. Qin, F. Li, K. Wang, Y. Han and C. Gao, Associated lattice and electronic structural

evolutions in compressed multilayer ReS_2, *J. Phys. Chem. Lett.*, 2017, **8**(15), 3648–3655.

22 S. Tong, J. Wang, Y. Yan, H. Liu, Y. Han and C. Gao, Emergence of electronic conduction in bismuth-oxide electrolyte under high pressure, *Jpn. J. Appl. Phys.*, 2019, **58**(6), 060913.

23 C. Zhou, J. Cao, H. Lin, B. Xu, B. Huang and S. Chen, Controllable synthesis and photocatalytic activity of Ag/BiOI based on the morphology effect of BiOI substrate, *Surf. Coat. Technol.*, 2015, **272**, 213–220.

24 K. Syassen, Ruby under pressure, *High Press. Res.*, 2008, **28**(2), 75–126.

25 Z. Kása, E. Orbán, Z. Pap, I. Ábrahám, K. Magyari, S. Garg and K. Hernadi, Innovative and cost-efficient BiOI immobilization technique on ceramic paper-total coverage and high photocatalytic activity, *Nanomaterials*, 2020, **10**(10), 1959.

26 F. Ke, C. Liu, Y. Gao, J. Zhang, D. Tan, Y. Han, Y. Ma, J. Shu, W. Yang, H. Mao, X. Chen and C. Gao, Interlayer-glide-driven isosymmetric phase transition in compressed In_2Se_3, *Appl. Phys. Lett.*, 2014, **104**(21), 212102.

27 K. Liu, L. Dai, H. Li, H. Hu, L. Yang, C. Pu, M. Hong and P. Liu, Phase transition and metallization of orpiment by Raman spectroscopy, electrical conductivity and theoretical calculation under high pressure, *Materials*, 2019, **12**(5), 784.

28 K. Kamali, K. Ananthasivan, T. R. Ravindran and D. S. Kumar, High pressure Raman spectroscopic studies on nanocrystalline ThO_2, *J. Nucl. Mater.*, 2017, **493**, 77–83.

29 J. C. Abrantes, J. A. Labrincha and J. R. Frade, An alternative representation of impedance spectra of ceramics, *Mater. Res. Bull.*, 2000, **35**(5), 727–740.

30 H. Zhang, F. Ke, Y. Li, L. Wang, C. Liu, Y. Zeng, M. Yao, Y. Han, Y. Ma and C. Gao, Anomalous Structural Transition and Electrical Transport Behaviors in Compressed Zn2SnO4: Effect of Interface, *Sci. Rep.*, 2015, **5**(1), 1–8.

31 L. Zhao, H. Liu, S. Tong, J. Wang, T. Han, C. Liu, C. Gao and Y. Han, Application of impedance spectroscopy in exploring electrical properties of dielectric materials under high pressure, *J. Phys.: Condens. Matter*, 2022, **34**, 434001.

32 C. Liu, Y. Sui, W. Ren, B. Ma, Y. Li, N. Su, Q. Wang, Y. Li, J. Zhang, Y. Han, Y. Ma and C. Gao, Electrical properties and behaviors of cuprous oxide cubes under high pressure, *Inorg. Chem.*, 2012, **51**(13), 7001–7003.

33 Q. Wang, D. Sang, H. Jiao, C. Liu, W. Wang, Y. Han, Y. Ma and C. Gao, Ionic transport and dielectric properties in $NaNbO_3$ under high pressure, *Appl. Phys. Lett.*, 2017, **111**(15), 152903.

34 T. Qin, Q. Wang, L. Wang, H. Yan, C. Liu, Y. Han, Y. Ma and C. Gao, High-pressure dielectric behavior of $BaMoO_4$: a combined experimental and theoretical study, *Phys. Chem. Chem. Phys.*, 2016, **18**(48), 33109–33114.